Available online at www.sciencedirect.com
ScienceDirect
International Journal of Thermal Sciences 45 (2006) 1140–1148
International Journal of Thermal Sciences
www.elsevier.com/locate/ijts

A numerical study of laminar convective heat transfer in microchannel with non-circular cross-section ☆

Li Zhuo, Tao Wen-Quan *, He Ya-Ling

State Key Laboratory of Multiphase Flow in Power Engineering Xi'an Jiaotong University, Xi'an 710049, China

Received 10 September 2005; accepted 21 January 2006

Available online 21 August 2006

Abstract

Three-dimensional numerical simulations of the laminar flow and heat transfer of water in silicon microchannels with non-circular cross-sections (trapezoidal and triangular) were performed. The finite volume method was used to discretize the governing equations. Numerical results were compared with experimental data available in the literature, and good agreements were achieved. The effects of the geometric parameters of the microchannels were investigated, and the variations of Nusselt number with Reynolds number were discussed from the field synergy principle. The simulation results indicate that when the Reynolds numbers are less than 100, the synergy between velocity and temperature gradient is much better than the case with Reynolds number larger than 100. There is an abrupt change in the intersection angle between velocity and temperature gradient around $Re = 100$. In the low Reynolds number region the Nusselt number is almost proportional to the Reynolds number, while in the high Reynolds number region, the increasing trend of Nusselt number with Reynolds number is much more mildly, which showed the applicability of the field synergy principle. In addition, for the cases studied the fully developed Nusselt number for the microchannels simulated increases with the increasing Reynolds number, rather than a constant.

Keywords: Numerical simulation; Laminar flow; Heat transfer; Microchannel; Field synergy principle

1. Introduction

Due to the rapid growth of technology applications which require heat transfer at high rates in relatively small spaces and volumes, the ability to remove heat from the high heat flux region becomes an important factor in designing reliable microsystems. Microchannel has the attributes of high surface area to volume ratio, large convective heat transfer coefficient, small mass and volume, etc. All of the attributes make it possible to cool such devices by micro-heat sinks, to produce micro-biochips and mini-compact heat exchangers developed in recent years. Because of the limited heat transfer ability of air-cooling technique, researchers show more interest in microchannel liquid-cooling technique. In the early 1980s, Tuckermann and Pease [1] introduced the heat sink concept of microchannel. To develop an optimization design scheme of such microsystem it is essential to have an accurate description of the transport processes. Since it is very difficult to get an analytical solution, developing a numerical method becomes necessary. Weisberg et al. [2] numerically analyzed a two-dimensional conjugate heat transfer problem in microchannel. Fedorov et al. [3] studied the three-dimensional conjugate heat transfer in the microchannel heat sink for electronic packaging. In these papers, the incompressible laminar Navier–Stokes equations of fluid motion were employed and the governing conservation equations were numerically solved using the generalized single equation framework for solving conjugated problems. Toh et al. [4] reported numerical results based on the experimental conditions of Tuckermann [5]. Fedorov and Viskanta [6] reported numerical results based on the experiments of Kawano et al. [7]. Using the FVM, they predicted the friction and thermal resistance which agreed well with the results of [7].

☆ A preliminary version of this paper was presented at ICMM05: Third International Conference on Microchannels and Minichannels, held at University of Toronto, June 13–15, 2005, organized by S.G. Kandlikar and M. Kawaji, CD-ROM Proceedings, ISBN: 0-7918-3758-0, ASME, New York.

* Corresponding author.
E-mail address: wqtao@mail.xjtu.edu.cn (W.-Q. Tao).

1290-0729/$ – see front matter
doi:10.1016/j.ijthermalsci.2006.01.011

Nomenclature

D	hydraulic diameter of microchannel	μm
BH	height of silicon-wafer	μm
H	height of microchannel	μm
L	length of microchannel	μm
W	width of computation domain	μm
W_b	bottom width of microchannel	μm
W_t	top width of microchannel	μm
h	heat transfer coefficient	$W m^{-2} K^{-1}$
k	conductivity	$W m^{-1} K^{-1}$
c_p	specific heat at constant pressure	$J kg^{-1} K^{-1}$
P	pressure	Pa
T	temperature	K
T_{in}	inlet temperature	K
$\vec{U}$	vector of velocity	$m s^{-1}$
U	velocity	$m s^{-1}$
u, v, w	velocity in x, y, z directions	$m s^{-1}$
w_{in}	inlet velocity	$m s^{-1}$
q	heat flux	$W m^{-2}$
m	mass flow rate	$kg s^{-1}$
Re	Reynolds number	
Pr	Prandtl number	
Nu	Nusselt number	
N	number of grid	
f	friction factor	

Greek symbols

ρ	density	$g m^{-3}$
μ	dynamic viscosity	Pa s
θ	microchannel angle	°
β	angle between U and ∇T	°
δ_t	thermal boundary layer thickness	m
Γ	interface between solid and liquid	
Φ	heat source	$W m^{-3}$

Subscripts

b	bottom of microchannel
l	liquid
in	at inlet of microchannel
s	solid
t	top of microchannel
w	value on the wall surface
∞	value at great distance from a body
th	thermal entrance
x	based on width
z	based on length

Wu and Cheng [8] conducted the experimental study of convective heat transfer in silicon microchannel with different surface conditions. It is found that the values of Nusselt number and apparent friction coefficient depend greatly on different geometric parameters. The laminar Nusselt number and apparent friction coefficient increase with the increase of surface roughness and surface hydrophilic property. The experimental results show that the Nusselt number increases almost linearly with the Reynolds number at low Reynolds number ($Re < 100$), While if the Reynolds number is greater than 100 the increasing rate of Nu with Re gradually decreases. The channels used in their experiment are integrated in silicon-base, which is a common practice for MEMS. Thus a better understanding of the fluid flow and heat transfer characteristics for such case is crucial for the development of compact, efficient, and reliable microsystems.

In this paper, a detailed numerical study was conducted based on the experimental conditions of Wu and Cheng [8]. The FVM (finite-volume-method) was used to solve the discretized governing equations for water flow and heat transfer in the microchannels. The thermal properties of water are assumed to be constants except the viscosity varying with temperature. The predicted thermal resistances are compared with their experimental data and quite good agreements are obtained. A detailed description of the heat sink temperature distribution, heat transfer coefficients in the developing region and fully developed region are presented and discussed. Furthermore, by using the field synergy principle the experimental results are discussed.

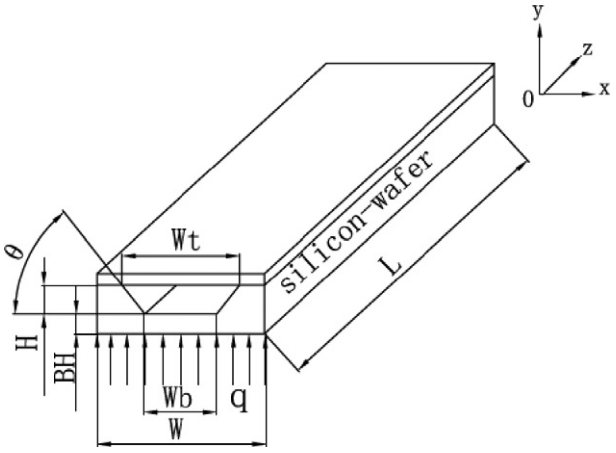

Fig. 1. Schematic of physical arrangement and the coordinate system.

2. Numerical analysis

2.1. Assumptions of physical model

In this paper, the fluid flow and heat transfer in a three-dimensional symmetric microchannel (Fig. 1) is simulated. The geometry dimensions were copied from the experimental work by Wu and Cheng [8]. The channels were heated from their bottom as shown in Fig. 2. The entire rectangular section is taken as the computational region (shown by the dash-lines in Fig. 2) with conjugated method [9]. Two sets of geometric parameters of microchannels were adopted (Table 1). The simulations were performed based on the following assumptions:

Table 1
Geometric parameters for microchannels (unit: length: μm, angle: degree)

No.	W_t	W	W_b	H	BH	L	D	θ
#1	770.5	1541	672.6	56.34	30	30500	102	49
#2	171.7	343.4	0	110.1	6	30500	84	52

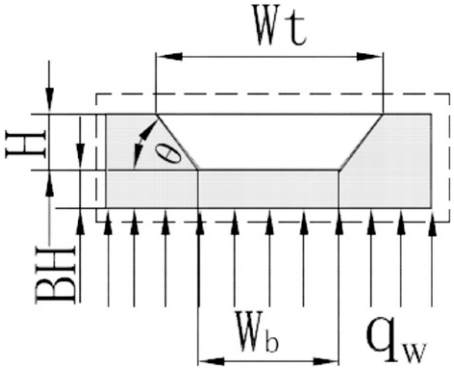

Fig. 2. Cross-section of microchannel.

(1) The governing equations based on Navier–Stokes equations can be used to describe the physical processes.
(2) The process is steady and the fluid is incompressible.
(3) The flow is laminar.
(4) The body forces are neglected.
(5) The left and right sides and the top of the channel are adiabatic.
(6) The thermal properties of solid and water are constants except the water viscosity varying with the temperature.

2.2. Governing equations

According to the above assumptions, the 3D Navier–Stokes and energy equations are used to describe the fluid flow and heat transfer in the whole region including fluid and solid. The governing equations are:

Continuity:

$$\rho_l \nabla \cdot \vec{U} = 0 \tag{1}$$

Momentum:

$$\rho_l(\vec{U} \cdot \nabla \vec{U}) = -\nabla P + \nabla \cdot (\mu_l \nabla \vec{U}) \tag{2}$$

Energy:

$$\rho_l c_{p,l}(\vec{U} \cdot \nabla T) = k_l \nabla^2 T \tag{3}$$

The solid material is silicon and the thermal conductivity is taken as 148 W $(m^{-1}K^{-1})$.

2.3. Boundary conditions

The inlet velocity is given at the micro-channel inlet:

$$z = 0, \qquad w = w_{\text{in}}, \qquad u = 0, \qquad v = 0 \tag{4}$$

The outlet boundary condition is assumed to be fully developed [9]:

$$z = L, \qquad \frac{\partial u}{\partial z} = 0, \qquad \frac{\partial v}{\partial z} = 0, \qquad \frac{\partial w}{\partial z} = 0 \tag{5}$$

The velocities in the solid region are zero which are guaranteed by our numerical solution algorithm for the conjugated problem [9] and no special conditions should be added for the solid–liquid interfaces since they are a part of the computational domain. The velocity no-slip condition at the solid surface can be automatically satisfied by our numerical method.

The thermal boundary conditions are given as follows. The boundary conditions of the left and right sides the computational domain are adiabatic:

$$x = 0, \qquad -k_w \frac{\partial T_w}{\partial x} = 0 \tag{6}$$

$$x = W, \qquad -k_w \frac{\partial T_w}{\partial x} = 0 \tag{7}$$

At the bottom position, the heat flux is given as shown in Fig. 2, and the top is adiabatic:

$$y = 0, \qquad -k_w \frac{\partial T_w}{\partial y} = q_w \tag{8}$$

$$y = H + BH, \qquad -k_w \frac{\partial T_w}{\partial y} = 0 \tag{9}$$

At the inlet position, the inlet temperature of liquid is given, and the outlet is assumed to be fully developed:

$$z = 0, \qquad T_l = T_{\text{in}} \tag{10}$$

$$z = L, \qquad \frac{\partial T_l}{\partial z} = 0 \tag{11}$$

As indicated above the entire region (include the solid one) was treated as the computational domain, hence the computations is of conjugated type. The numerical algorithm is well documented in literature [9], and will not be re-stated here.

The relation between viscosity and temperature of deionized water is [10]:

$$\mu_l = 2.414\text{E}{-}05 \times 10^{247.8/(T-140.0)} \tag{12}$$

2.4. Numerical method

In this paper, a self-developed code was used. The FVM (finite-volume-method) [9,11] was used to discretize the governing equations with the boundary conditions in rectangular Cartesian coordinates and the grid was cuboid. The staggered grid system was used. The differential equations were integrated over each control volume to derive the discretized equation. The QUICK scheme was applied to the convective term, and the central second order differencing scheme for was used for the diffusion terms. The CLEAR algorithm [12,13] with under-relaxation iterative methods is adopted to solve the resulting system of equations in primitive variables, namely u, v, w, p, T. If the relative mass unbalance in the entire domain is less than 10^{-6}, the iteration is terminated. The grid system

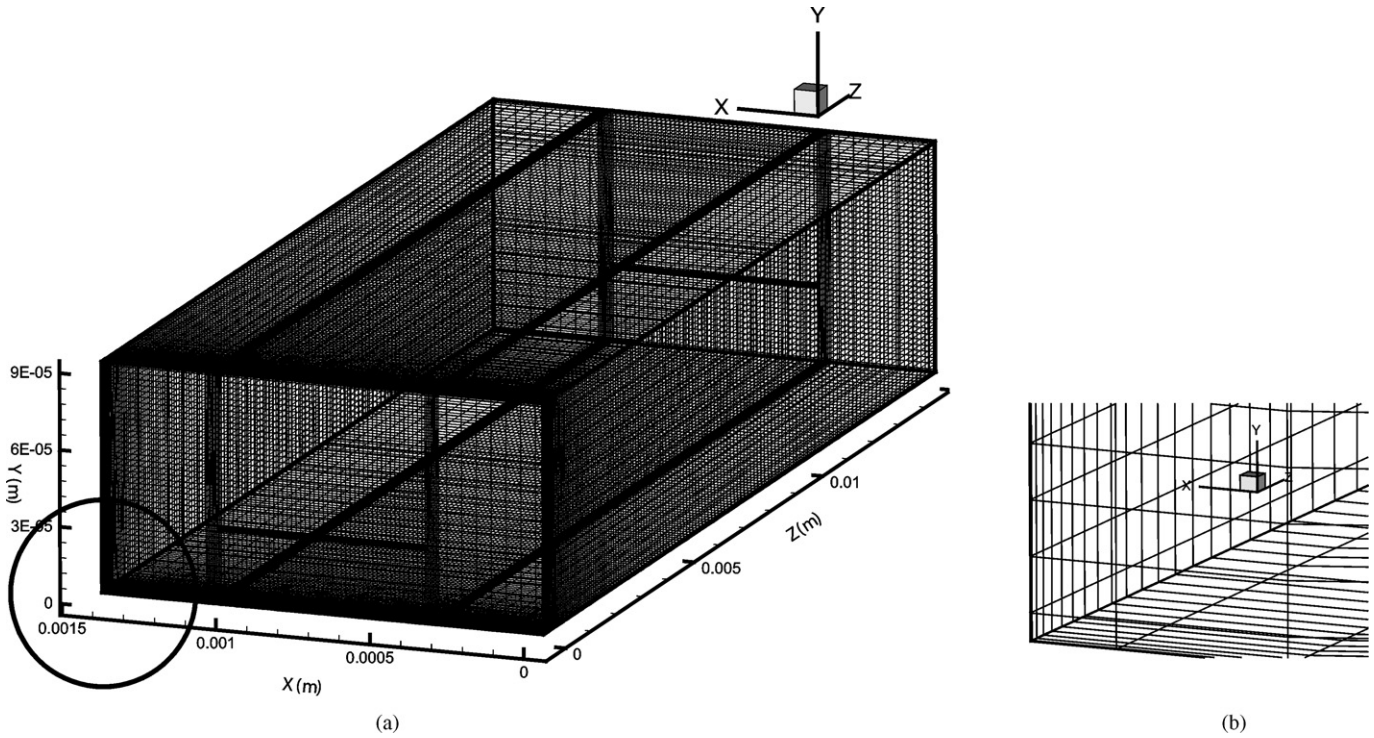

Fig. 3. (a) Nonuniform grid generated of microchannel (for #1). (a) far-off view; (b) close-up of the grid at one of the corners.

used in this paper was $82(x)$, $42(y)$ and $142(z)$ for both microchannels. The gird system of microchannel #1 was shown in Fig. 3. This system was adopted after a grid-independence examination. A non-uniform grid arrangement was applied in x and z directions. In x direction, the grid distribution was finer in the liquid region especially near the channel corner, while in z direction, more grids were arranged in the inlet region. In the computations the water inlet temperature was 293 K and $q_w = 10^6\ \mathrm{W\,m^{-2}}$. The Reynolds numbers range from 30 to 400.

3. Results and discussion

3.1. Outlet velocity distributions

Fig. 4 shows the outlet velocity of microchannel #1 and Fig. 5 shows the outlet velocity of microchannel #2 for $Re = 60$. Since the viscosity varies with temperature, the values of Reynolds number are based on the outlet condition. These pictures present the fully developed patterns of the axial outlet velocity.

3.2. Local temperature distributions

The temperature distributions at four cross-sections along the microchannel #1 are shown in Fig. 6. It is obvious that the isotherms in the fluid are closer than that in the solid because of different thermal conductivity. At the inlet the local heat transfer rate is the highest, and it soon decreases along the z direction as indicated by the fact that the isothermal distribution becomes coarser and coarser along the flow direction.

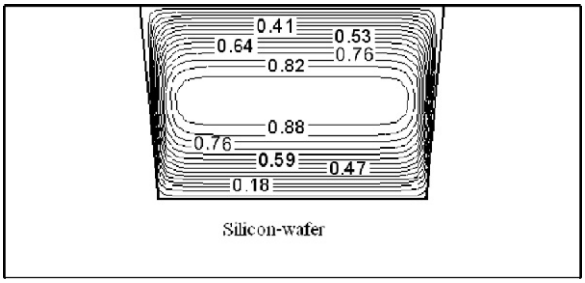

Fig. 4. Velocity distribution of microchannel #1 at outlet, $Re = 60$.

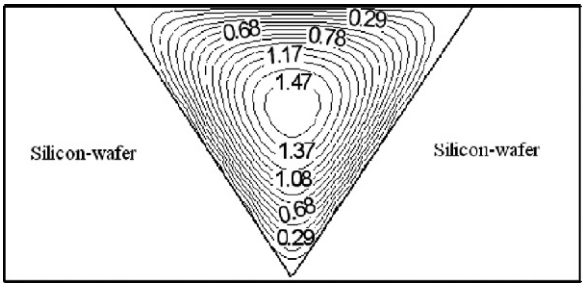

Fig. 5. Velocity distribution of microchannel #2 at outlet, $Re = 60$.

Fig. 7 shows the temperature distributions of microchannel #2 at four cross-sections along the flow direction, and the same variation trend can be observed. In Figs. 8 and 9, the temperature distributions at the y–z plane of channels #1 and #2 with $x = L_x/2$ are presented. From the figures, it can be clearly observed that the intensity of heat transfer between solid and fluid is the highest at the microchannel inlet and decreases along flow direction.

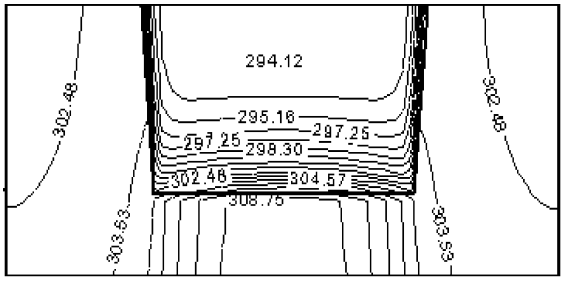

(a) z/L_z=1/30

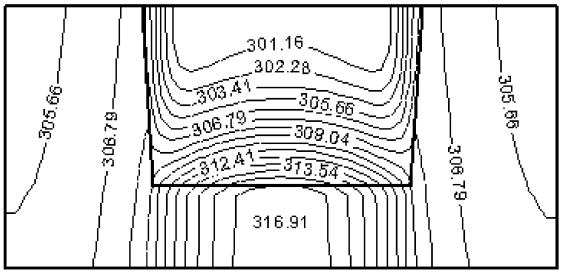

(b) z/L_z=1/3

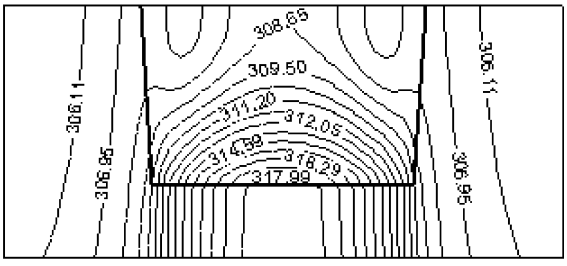

(c) z/L_z=2/3

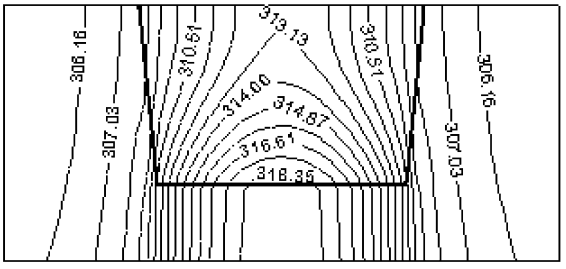

(d) z/L_z=1

Fig. 6. Temperature distribution (in Kelvins) at four different cross-sections along z direction of microchannel #1, $Re = 60$.

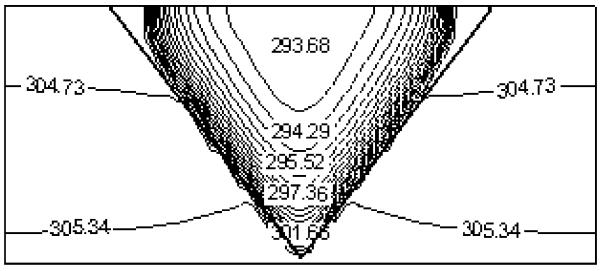

(e) z/L_z=1/30

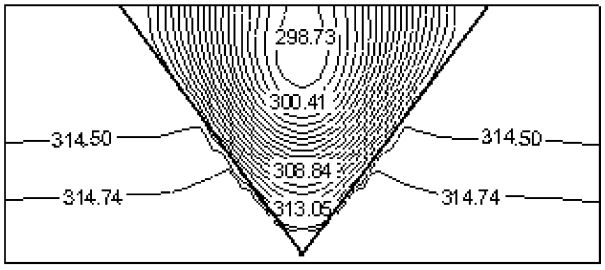

(f) z/L_z=1/3

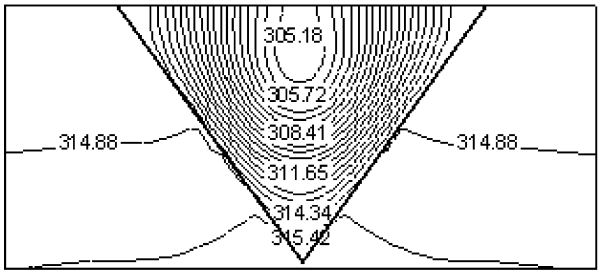

(g) z/L_z=2/3

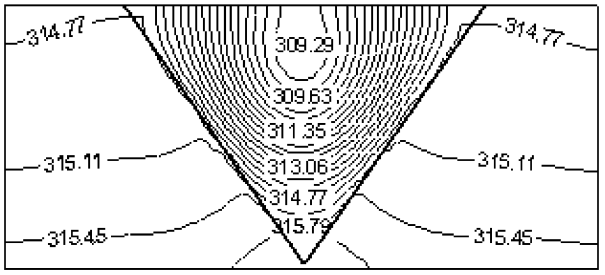

(h) z/L_z=1

Fig. 7. Temperature distribution (in Kelvins) at four different cross-sections along z direction of microchannel #2, $Re = 60$.

3.3. Average heat transfer characteristics

In order to evaluate the local heat flux distributions at the liquid–solid interface along the water flow direction, the local heat transfer coefficients and local Nusselt numbers must be defined. The definitions of the local heat transfer coefficient and the Nusselt number definition for the strong conjugate heat transfer problem suggested in [14] were adopted:

$$h_{z,\mathrm{ave}} = \frac{\bar{q}_{s,\Gamma(z)}}{\Delta T_z} \tag{13}$$

$$Nu_{z,\mathrm{ave}} = \frac{h_{z,\mathrm{ave}} \cdot D}{k_l} \tag{14}$$

The averaged local heat flux along the perimeter of the inner surface of the channel is defined as:

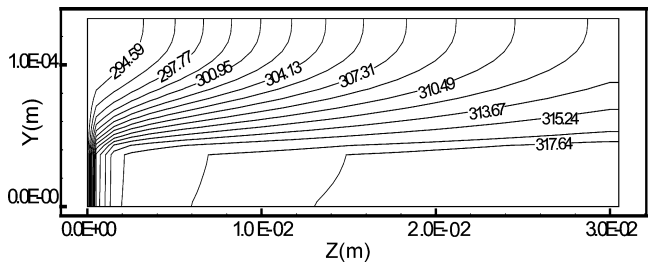

Fig. 8. Temperature (in Kelvins) distribution along z direction of microchannel #1 at $x = L_x/2$, $Re = 60$.

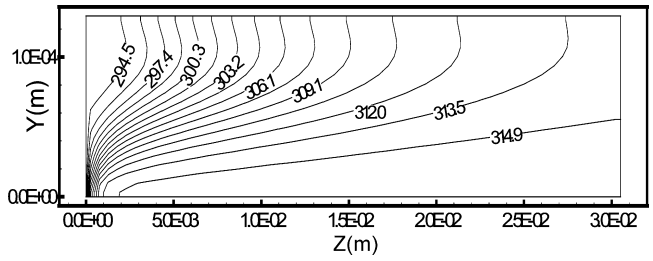

Fig. 9. Temperature (in Kelvins) distribution along z direction of microchannel #2 at $x = L_x/2$, $Re = 60$.

$$\bar{q}_{s,\Gamma(z)} = -k_w\left(\frac{\partial T_w(x,y,z)}{\partial n}\bigg|_{\Gamma}\right) = -k_l\left(\frac{\partial T_l(x,y,z)}{\partial n}\bigg|_{\Gamma}\right) \quad (15)$$

$$\Delta T_z = \frac{(\Delta\overline{T}(z) - \Delta\overline{T}_{\text{ave}})}{\ln(\Delta\overline{T}(z)/\Delta\overline{T}_{\text{ave}})} \quad (16)$$

where

$$\Delta\overline{T}(z) = \overline{T}_{w,\Gamma(z)} - \overline{T}_{l(z)} \quad (17)$$

$$\Delta\overline{T}_{\text{ave}} = \overline{T}_{w,\text{ave}} - \overline{T}_{l,\text{ave}} \quad (18)$$

$\overline{T}_{w,\text{ave}}$, $\overline{T}_{l,\text{ave}}$ are averaged values from $\overline{T}_{w,\Gamma(z)}$, $\overline{T}_{l(z)}$, respectively. The definitions of $\overline{T}_{w,\Gamma(z)}$, $\overline{T}_{l(z)}$ are:

$$\overline{T}_{w,\Gamma(z)} = \frac{\sum_{\Gamma} T_{w,\Gamma(i,j,k)}}{N_{\Gamma}} \quad (19)$$

$$\overline{T}_{l(z)} = \frac{\sum\sum \rho_l \cdot w(i,j) \cdot c_p \cdot T_{l(i,j,k)} \Delta x \Delta y}{\dot{m}_{\text{num}} \cdot c_p} \quad (20)$$

where N_{Γ} is the total number of nodes along perimeter of the inner surface (here, $N_{\Gamma} = 2 \times 30 + 50$). The definition of $\dot{m}_{\text{num}}$ is:

$$\dot{m}_{\text{num}} = \sum\sum \rho_l \cdot w(i,j) \Delta x \Delta y \quad (21)$$

$$\overline{T}_{w,\text{ave}} = \frac{\sum \overline{T}_{w,\Gamma(z)}}{N_z} \quad (22)$$

$$\overline{T}_{l,\text{ave}} = \frac{\sum \overline{T}_{l(z)}}{N_z} \quad (23)$$

where N_z is the number of nodes along the flow direction (here, $N_z = 140$). As for the heat transfer coefficient and Nusselt number in the fully developed region, both of them are constants and the temperature difference is defined as follows:

$$\Delta T_z = \overline{T}_{w,\Gamma(z)} - \overline{T}_{l(z)} \quad (24)$$

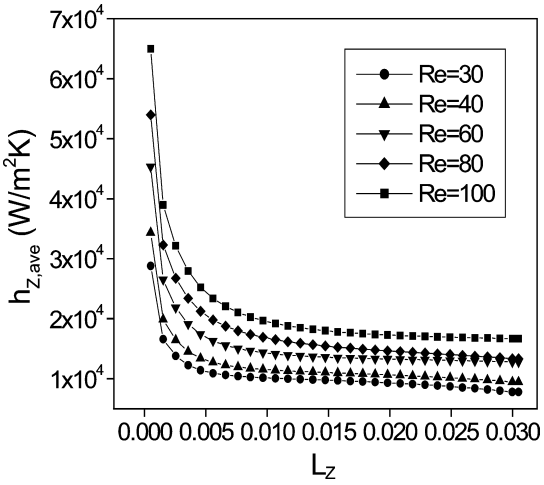

Fig. 10. Longitudinal heat transfer coefficients variation for various *Re* numbers of microchannel #1.

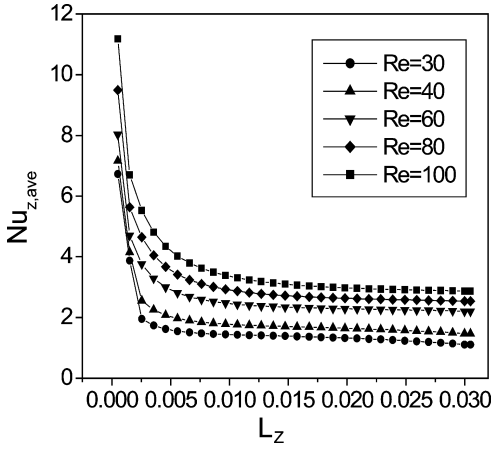

Fig. 11. Longitudinal *Nu* numbers variation for various *Re* numbers of microchannel #1.

where $\overline{T}_{w,\Gamma(z)}$, $\overline{T}_{l(z)}$ are the circumference average temperatures in fully developed region, and defined by Eqs. (19) and (20), respectively.

Figs. 10 and 11 show the variation of heat transfer coefficients and Nusselt numbers of microchannel #1, respectively, with the Reynolds number ranging from 30 to 100. Figs. 12 and 13 show the results of microchannel #2. It can be clearly observed that at the inlet the local heat transfer intensity is very high, and the heat transfer intensity decreases with the fluid going downstream gradually approaching a constant, just as in a channel with a conventional dimension. The thermal entry lengths of a circular tube can be estimated by Incropera and DeWitt [15]:

$$L_{\text{th}} = 0.05 Re\, Pr\, d \quad (25)$$

For the non-circular cross-section duct studied in this paper, the thermal entry lengths can be estimated by replacing the tube diameter d in Eq. (25) with the hydraulic diameter D. For both microchannels, assuming $Pr = 7.0$, Reynolds numbers ranging from 30 to 100, we can obtain the corresponding results. For microchannel #1, the lengths are 1.07, 1.43, 2.29, 3.06 and 3.57 mm, respectively; For microchannel #2, the lengths are

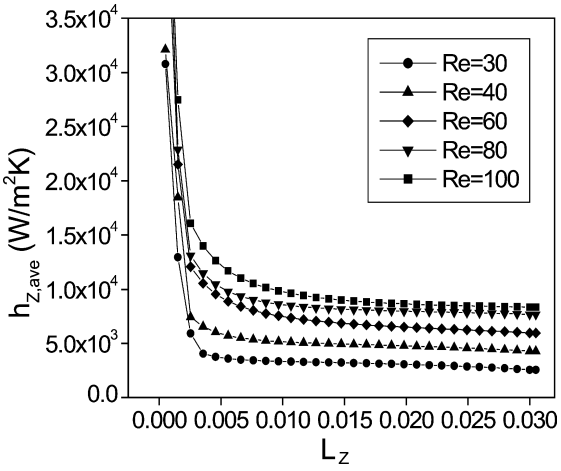

Fig. 12. Longitudinal heat transfer coefficients variation for various *Re* numbers of microchannel #2.

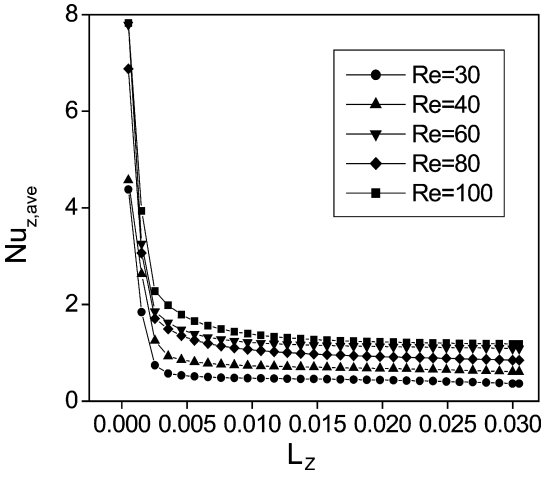

Fig. 13. Longitudinal *Nu* numbers variation for various *Re* numbers of microchannel #2.

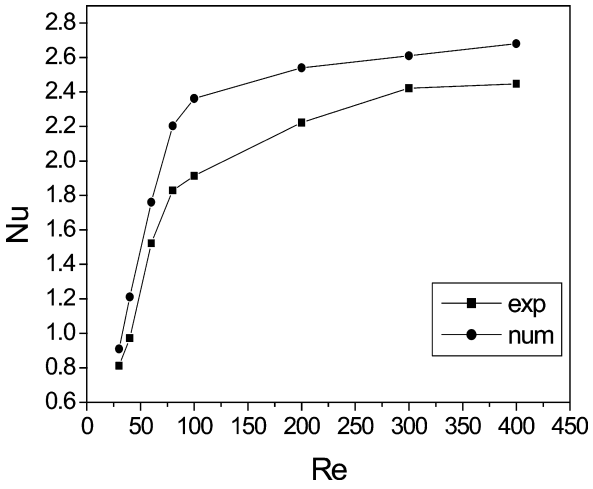

Fig. 14. Fully developed region *Nu* numbers for experiment and numerical simulation of microchannel #1.

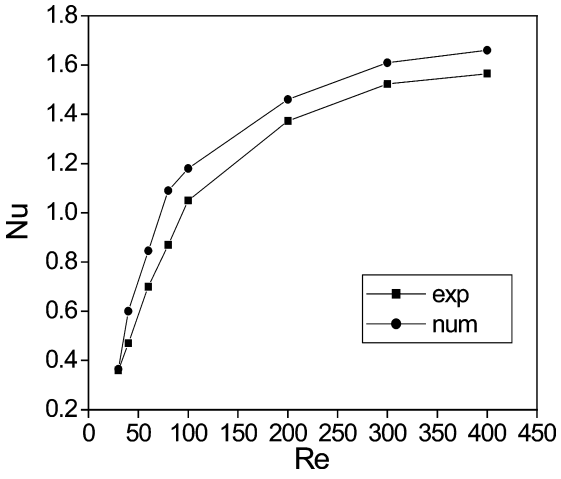

Fig. 15. Fully developed region *Nu* number for experiment and numerical simulation of microchannel #2.

0.88, 1.17, 1.76, 2.35 and 2.93 mm, respectively. Comparing the above results with the Figs. 10, 11, 12 and 13, it can be seen that the estimated length of the fully developed region by Eq. (25) is much less than the numerical results. Thus the entrance length of microchannel fluid flow and heat transfer is a problem open to discussion. From the numerical results it can be found that after the fluid flows a long-enough pass, the local heat transfer coefficient becomes constant, indicating the occurrence of fully developed regime. In the following the attention will be paid for the characteristics of the fully developed region.

In order to compare the numerical simulation results with the experimental results, a wide range Reynolds number ($30 \leqq Re \leqq 400$) for the periodic fully developed convective heat transfer is simulated ($30 \leqq Re \leqq 400$). The Nusselt numbers for both microchannels in the fully developed region are obtained and the variations of Nusselt number with Reynolds number are shown in Figs. 14 and 15, where the experimental results [8] are also presented for comparison. Numerical results show that when $Re < 100$, the Nusselt number increases with the Reynolds number almost linearly. While at larger Reynolds numbers, the Nusselt numbers increase much more mildly, which agrees well with the experimental result.

In Fig. 14, there is an appreciable difference between numerical simulation and experimental data [8]. This deviation may come from the difference in the data reduction: in the numerical simulation the average wall temperatures were computed from the three solid surfaces of the microchannel while in the experiment only the bottom wall temperature was computed; furthermore, the liquid local temperature were computed from the actual temperature distribution in the numerical simulation, while in the experiment the linearly interpolation of inlet and outlet liquid temperature was applied to deduce the liquid local temperature which is very difficult to obtain in the microchannel experiment.

From Figs. 10 and 12, it can be clearly observed that the heat transfer coefficients of the fully developed region of the trapezoidal channel is appreciably larger than those of the triangle channel, indicating a strong effect of the cross section geometry on the heat transfer characteristics of microchannel heat transfer.

3.4. Further discussion

The field synergy principle is a novel concept of heat transfer enhancement [16,17]. As shown in [17] the general 3D energy equation:

$$\rho c_p\left(u\frac{\partial T}{\partial x}+v\frac{\partial T}{\partial y}+w\frac{\partial T}{\partial z}\right) = k\left(\frac{\partial^2 T}{\partial x^2}+\frac{\partial^2 T}{\partial y^2}+\frac{\partial^2 T}{\partial z^2}\right)+\dot{\Phi} \tag{26}$$

can be re-written into the following form by integration of it over the entire computational domain:

$$\int_{\Omega}\left[\rho c_p\left(u\frac{\partial T}{\partial x}+v\frac{\partial T}{\partial y}+w\frac{\partial T}{\partial z}\right)-k\left(\frac{\partial^2 T}{\partial x^2}+\frac{\partial^2 T}{\partial z^2}\right)-\dot{\Phi}\right]\mathrm{d}\Omega = -k\frac{\partial T}{\partial y}\bigg|_w \tag{27}$$

where Ω is the computational domain and $\dot{\Phi}=0$ (without internal heat source). The thermophysical properties ρ, c_p are assumed constants. For liquids with Peclet number greater than 100, the heat conduction in the liquids can be neglected compared with the convection term [18], and the term $-k\frac{\partial T}{\partial y}|_w$. represents the fluid conduction term along the solid wall. Thus we have:

$$\int_{\Omega}(U\cdot\nabla T)\,d\Omega = -k\frac{\partial T}{\partial y}\bigg|_w \tag{28}$$

The vector dot product, $U\cdot\nabla T$ in the dimensional integration in Eq. (28) can be expressed as:

$$U\cdot\nabla T = |U||\nabla T|\cos\beta \tag{29}$$

where β is the intersection angle (synergy angle) between the velocity and the temperature gradient(heat flow vector). Eq. (29) shows that in the convection domain there are two vector fields, U and ∇T, or three scalar fields, $|U|$, $|\nabla T|$ and $\cos\beta$. It is obvious that the value of the integration or the strength of the convection heat transfer depends not only on the velocity, the temperature gradient, but also on their synergy. Thus it can be seen that for the same other conditions, the smaller the synergy angle the larger the heat transfer rate, and this is one of the major concepts of the field synergy principle for which details can be found in [16,18,19].

In order to have a deep understanding of the experimental fact that the Nusselt number increases almost linearly with the Reynolds number at low Reynolds number ($Re<100$), the volume averaged synergy angle for the two microchannels flow in the fully developed region were determined. Fig. 16 shows that the synergy angle β varies with Reynolds number. It can be clearly observed that below $Re=100$, the synergy angle is much less than that for the region of $Re>100$. It should be noted that in the range of 80–90 degree, a small difference in the angle will lead to a significant difference in its cosine value. For example, from the numerical results of microchannel #1, for $\beta=84^\circ$ ($Re=10$), $\cos\beta=0.105$, while for $\beta=89^\circ$ ($Re=150$), $\cos\beta=0.0174$. Therefore, qualitatively, the high heat transfer intensity at the low Reynolds number region can be explained by the better synergy between velocity and temperature gradient.

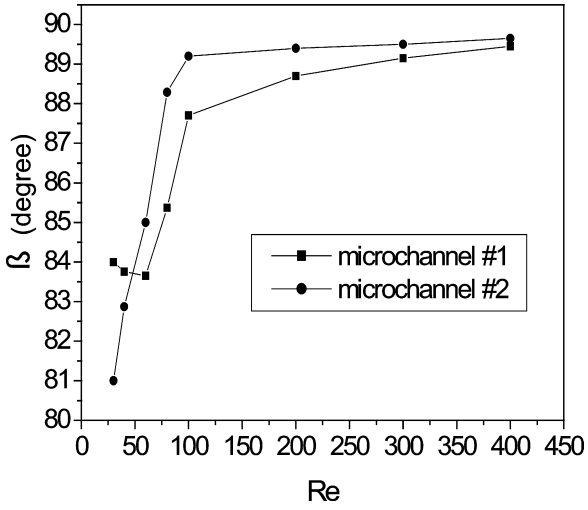

Fig. 16. Synergy angle various with *Re* number.

4. Conclusions

From the results and analysis of the present numerical simulation, following conclusions can be obtained:

(1) For liquid flow in microchannel sized to a hydraulic diameter of tens of micrometer, the Navier–Stokes and energy equations and the no-slip boundary condition based on the continuum assumption are still valid and can be used to predict the flow and heat transfer characteristics with reasonable accuracy.
(2) The heat transfer coefficients reduced from different definitions of the solid wall temperature may lead to a significant deviation between test data and the simulation results. Therefore, when the comparison is conducted between test and the simulation results, the same definition must be adopted in order to have a reasonable conclusion.
(3) For fully developed heat transfer of the two microchannels simulated, the synergy between velocity and temperature gradient in the low Reynolds number region ($Re<100$) is better than that of the region with $Re>100$, leading to a big difference in the variation slope of *Nu* vs. *Re* curve in the two regions.
(4) For the two microchannels simulated the heat transfer intensity of the trapezoidal microchannel is much better than that of the triangular microchannel, indicating the great effect of the geometric condition in microchannel system.
(5) For the two microchannels simulated, the Nusselt number in the fully developed region increases with the increasing in Reynolds number, seemingly different from that of conventional duct, where the Nusselt number of the fully developed laminar heat transfer is a constant. More study is underway in the authors' group in order to reveal the basic reasons.

Acknowledgements

This work is supported by the NNSFC (No. 50476046, 50236010) and the Research Foundation of Doctoral Projects of the Chinese Ministry of Education (RFDP20030698015).

References

[1] D.B. Tuckermann, R.F.W. Pease, High-performance heat sinking for VLSI, IEEE Electron. Edv. Lett. EDL 2 (1981) 126–129.
[2] A. Weisberg, H. Bau, J. Zemel, Analysis of microchannels for integrated cooling, Int. J. Heat Mass Transfer 35 (1992) 2465–2474.
[3] A.G. Fedorov, R. Viskanta, Three-dimensional conjugate heat transfer in the microchannel heat sink for electronic packaging, Int. J. Heat Mass Transfer 43 (2000) 399–415.
[4] K.C. Toh, X.Y. Chen, J.C. Chai, Numerical computation of fluid flow and heat transfer in microchannels, Int. J. Heat Mass Transfer 45 (2002) 5133–5141.
[5] D.B. Tuckermann, Heat transfer microstructures of investigated circuits, PhD thesis, Stanford University, 1984.
[6] A.G. Fedorov, R. Viskanta, Three-dimensional conjugate heat transfer in the microchannel heat sink for electronic packaging, Int. J. Heat Mass Transfer 43 (2000) 399–415.
[7] K. Kawano, K. Minakami, H. Iwasaki, M. Ishizuka, Development of microchannels heat exchanging, in: R.A. Nelson Jr, L.W. Swansin, M.V.A. Bianchi, C. Camci (Eds.), Application of Heat Transfer in Equipment, Systems, and Education, in: HTD, vol. 361-3/PID, vol. 3, ASME, New York, 1998, pp. 173–180.
[8] H.Y. Wu, P. Cheng, An experimental study of convective heat transfer in silicon microchannels with different surface conditions, Int. J. Heat Mass Transfer 46 (2003) 2547–2556.
[9] W.Q. Tao, Numerical Heat Transfer, second ed., Xi'an Jiaotong University Press, Xi'an, 2001.
[10] F. Incropera, Liquid Cooling of Electronic Devices by Single-Phase Convection, Wiley, New York, 1999.
[11] S.V. Patankar, Numerical Heat Transfer and Fluid Flow, Hemisphere, Washington, DC, 1980.
[12] W.Q. Tao, Z.G. Qu, Y.L. He, A novel segregated algorithm for incompressible fluid flow and hear transfer problems—CLEAR (Coupled & Linked Equations Algorithm Revised), Part I: Mathematical formulation and solution procedure, Numer. Heat Transfer B 45 (2004) 1–17.
[13] W.Q. Tao, Z.G. Qu, Y.L. He, A novel segregated algorithm for incompressible fluid flow and hear transfer problems—CLEAR (Coupled & Linked Equations Algorithm Revised), Part II: Application examples, Numer. Heat Transfer B 45 (2004) 19–48.
[14] J. Li, G.P. Peterson, P. Cheng, Three-dimensional analysis of heat transfer in a micro-heat sink with single phase flow, Int. J. Heat Mass Transfer 47 (2004) 4215–4231.
[15] F.P. Incropera, D.P. DeWitt, Fundamentals of Heat and Mass Transfer, fourth ed., Wiley, New York, 1996.
[16] Z.Y. Guo, D.Y. Li, B.X. Wang, A novel concept for convective heat transfer enhancement, Int. J. Heat Mass Transfer 41 (1998) 2221–2225.
[17] W.Q. Tao, Y.L. He, Z.G. Qu, F.Q. Song, A unified analysis on enhancing convective heat transfer with field synergy principle, Int. J. Heat Mass Transfer 45 (2002) 4871–4879.
[18] W.M. Kays, M.E. Crawford, Convective Heat and Mass Transfer, McGraw-Hill, New York, 1980, pp. 107, 246.
[19] Z.Y. Guo, W.Q. Tao, R.S. Shah, The field synergy (coordination) principle and its applications in enhancing single phase convective heat transfer, Int. J. Heat Mass Transfer 48 (2005) 1797–1807.